Modeling density segregation in flowing bidisperse granular materials

Hongyi Xiao[1], Paul B. Umbanhowar[1], Julio M. Ottino[1,2,3] and Richard M. Lueptow[1,3]

[1]Department of Mechanical Engineering,
[2]Department of Chemical and Biological Engineering, and
[3]The Northwestern University Institute on Complex Systems (NICO),
Northwestern University, Evanston, IL 60208, USA

Preventing segregation in flowing granular mixtures is an ongoing challenge for industrial processes that involve the handling of bulk solids. A recent continuum-based modeling approach accurately predicts spatial concentration fields in a variety of flow geometries for mixtures varying in particle size. This approach captures the interplay between advection, diffusion, and segregation using kinematic information obtained from experiments and/or discrete element method (DEM) simulations combined with an empirically determined relation for the segregation velocity. Here, we extend the model to include density-driven segregation, thereby validating the approach for the two important cases of practical interest. DEM simulations of density bidisperse flows of mono-sized particles in a quasi-2D bounded heap were performed to determine the dependence of the density-driven segregation velocity on local shear rate and particle concentration. The model yields theoretical predictions of segregation patterns that quantitatively match the DEM simulations over a range of density ratios and flow rates. Matching experiments reproduce the segregation patterns and quantitative segregation profiles obtained in both the simulations and the model, thereby demonstrating that the modeling approach captures the essential physics of density-driven segregation in granular heap flow.

THE ROYAL SOCIETY
PUBLISHING

1. Introduction

Granular materials with different particle properties tend to segregate spontaneously when they are flowing [1–4] or vibrating [5–7]. Such segregation is frequently encountered in industrial processes that involve handling bulk solids [8,9] as well as in geophysical transport such as debris flows [10], pyroclastic flows [11], and mineral transport [12]. Thus, modeling and predicting segregation is important, yet accurate models that can be broadly applied are only just now being developed.

Among different particle properties that can result in segregation, particle size [13] and density [14] are critical factors. The focus of this work is the segregation due to differences in particle density, which can occur in vibrated granular mixtures [15–19], free surface flows [20–24], and vertical chute flows [25]. In gravity-driven free surface flows, particles with lower density are more likely to rise to the free surface while particles with higher density are more likely to segregate to the bottom of the flowing layer, resulting in segregation patterns such as a segregated core or streaks of heavier particles in rotating tumblers [14,21–23]. While particle based simulation methods can reproduce density driven segregation phenomena on a small scale, an accurate continuum-based model would be of clear practical and theoretical value.

Over the years, continuum models for segregation in granular flows have been proposed for various geometries including plug [26–28], chute [24,29–35], and annular shear [36] flows, and some have achieved qualitative agreement with simulations and experiments. However, most of these studies focused on size segregation and have not been compared directly to simulations or experiments or have not convincingly been shown to provide accurate predictions. The underlying reasons include oversimplifying the kinematics of the flow, neglecting diffusion, or omitting the dependence of the segregation velocity on the local shear rate. Recently, Tripathi & Khakhar [20], Tunuguntla *et al.* [24], and Gray & Ancey [35] incorporated bidisperse density segregation into continuum models. These studies applied segregation velocities proportional to the normalized density difference and other parameters. Though the models showed a degree of agreement with simulations, validation of the segregation velocity or segregation patterns was lacking. We propose a different approach here and validate it by comparing predictions of this approach to both discrete element method (DEM) simulations and experiments.

In our recent work, we developed a continuum model based approach form predicting segregation of granular materials that achieves quantitative agreement with simulations and experiments of size bidisperse, multidisperse, and polydisperse granular materials in different geometries [37–40]. The model is based on the transport equation

$$\frac{\partial c_i}{\partial t} + \nabla \cdot (\boldsymbol{u} c_i) + \frac{\partial}{\partial z}(w_{s,i} c_i) - \nabla \cdot (D \nabla c_i) = 0, \tag{1.1}$$

which includes the affects of advection, segregation, and diffusion. Equation 1.1 is applied to the thin flowing layer (having length L and depth δ), where segregation occurs in most gravity driven flows. x is the streamwise direction ($0 < x < L$) and z is the normal direction ($-\delta < z < 0$), with $z = 0$ at the surface of the flowing layer. Terms with subscripts i represent the properties for species i in a bidispere mixture (h for heavy and l for light in the case of density segregation), while terms without subscripts represent the average flow properties of both species. The concentration of species i is defined as $c_i = f_i/f$, where f_i is the volume fraction for species i, and f is the total volume fraction of both species. $\boldsymbol{u} = u\hat{\boldsymbol{x}} + w\hat{\boldsymbol{z}}$ is the mean 2D velocity field, and D is the diffusion coefficient. The segregation velocity, $w_{s,i}$, is defined as the relative normal velocity component of species i with respect to the total normal velocity component of both species: $w_{s,i} = w_i - w$. In the segregation term $\frac{\partial}{\partial z}(w_{s,i} c_i)$, only flows normal to the free surface are considered, since segregation occurs primarily in this direction and the gradient of concentration in the streamwise direction is small. The model is informed by physical control parameters and kinematic parameters acquired from DEM simulations [39] or experiments. Thus, no fitting parameters are needed. While we consider the quasi-2D case here, the model can be extended to fully three-dimensional systems.
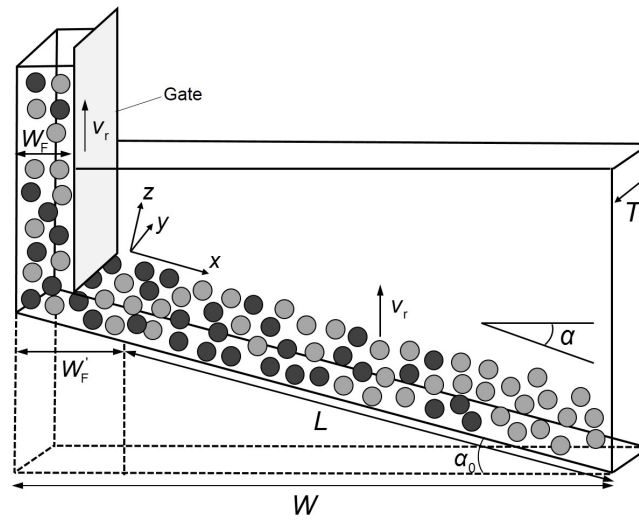
Figure 1. Schematic (not to scale) of a quasi-2D bounded heap for DEM simulations and experiments (with flowing layer length L and gap thickness T). In simulations, the bottom wall is inclined at an angle $\alpha_0 = 16°$ to reduce simulation time. The surface rise velocity, v_r, depends on the flow rate which is controlled by the vertical rise velocity of the gate located a distance W_F from the upstream wall.

In this research, this continuum model is used to predict the segregation of density bidisperse granular materials in a quasi-2D bounded heap, which typically exhibits complicated kinematics [41–44] with different segregation patterns including stratified layers of the two types of particles [45], fully segregated particles [46,47], and mixed particles with no segregation [48]. Here we study the continuous flow regime for which stratification does not occur [48]. DEM simulations are performed to determine the kinematics of density bidisperse flows and experiments are performed to verify the results of simulations and theoretical predictions. §2 describes the quasi-2D bounded heap geometry, the DEM simulation methods, and the experiments. In §3, we show that the simulations quantitatively reproduce the experimental results and discuss the flow kinematics. In §4, the continuum model (equation 1.1) is non-dimensionalized and solved numerically. The results are compared with simulation and experimental results for different cases, and the influence of physical control parameters on segregation is discussed. §5 presents the conclusions.

2. Simulation and experimental methods

(a) DEM simulations

In DEM simulations, the translational and rotational momenta of each particle are tracked using integration of Newton's Second Law. As in our previous work [37–39,44], the normal force model used in this research is the linear-spring dashpot model [49,50,52], in which the normal contact force between two particles is $\boldsymbol{F}_{ij}^n = \left[k_n\epsilon - 2\gamma_n m_{eff}(\boldsymbol{V}_{ij} \cdot \hat{\boldsymbol{r}}_{ij})\right]\hat{\boldsymbol{r}}_{/ij}$. In this relation, ϵ and $\boldsymbol{V}_{ij}$ represent the overlap and relative velocity between two contacting particles i and j, respectively. $\hat{\boldsymbol{r}}_{ij}$ is the unit normal vector between two particles, and $m_{eff} = m_i m_j/(m_i + m_j)$ denotes the effective mass. The normal stiffness k_n and damping γ_n are determined from the restitution coefficient e and binary collision time t_c: $k_n = [(\pi/t_c)^2 + \gamma_n^2]m_{eff}$ and $\gamma_n = -\ln e/t_c$, where ln is the natural logarithm. The tangential force model is the linear spring model with Coulomb friction [50], which can be expressed as $\boldsymbol{F}_{ij}^t = -\min(|k_s\beta|, |\mu\boldsymbol{F}_{ij}^n|)\text{sgn}(\beta)\hat{\boldsymbol{s}}$. Here, the tangential stiffness $k_s = \frac{2}{7}k_n$, and the tangential displacement is $\beta(t) = \int_{t_s}^t \boldsymbol{V}_{ij}^s dt$ [51], where t_s is the initial contact time and $\boldsymbol{V}_{ij}^s$ is the relative tangential velocity. μ denotes the friction coefficient.
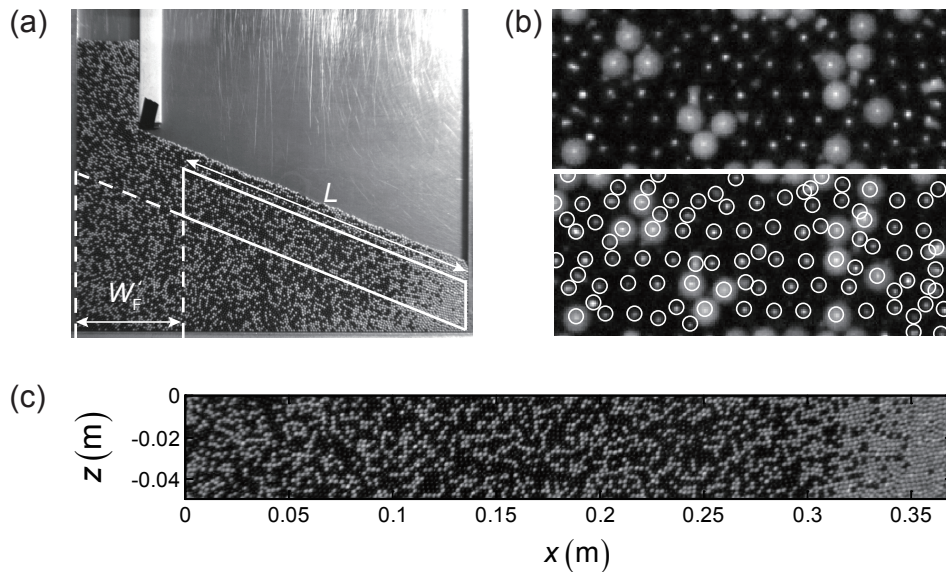
Figure 2. Image processing of frames captured by a high speed camera using steel (dark) and ceramic particles (white). (a) A portion (solid white box) of the original image is extracted that captures the final segregation pattern of particles deposited on the heap. (b) Particles are identified for the PTV algorithm in a close-up of the image. (c) Boxed region in (a) after rotating and shearing.

In real granular systems, materials with different densities ρ often have different surface and elastic properties. Here, to ensure that density is the only driving mechanism for segregation in simulations, identical material properties are applied except for the density. The binary collision time is $t_c = 10^{-3}$ s, which is small enough to accurately describe the flow of hard spheres [44]. The restitution coefficient is $e = 0.9$ and the friction coefficient is $\mu = 0.2$. These values are selected so that the dynamic repose angle α in simulations matches the dynamic repose angle in experiments. Negligible differences in segregation occur over a range of values for t_c, e, and μ, indicating that the simulations are relatively insensitive to the specific values used. The time step for the simulations is set to $t_c/40 = 2.5 \times 10^{-5}$ s, which ensures numerical stability [39].

A schematic of the simulation geometry is shown in figure 1. The quasi-2D bounded heap has width $W = 0.5$ m and gap thickness $T = 0.016$ m. To save computation time, the bottom wall is inclined at an angle $\alpha_0 = 16°$, which is smaller than the dynamic repose angle α (which ranges from $18°$ to $21°$ in different cases). Initially the bottom wall is covered with a layer of immobilized particles. After the particles flowing into the system form a 10-15 particle diameters thick layer, the velocity profiles and concentration profiles in the flowing layer become steady, indicating that the effect of the bottom wall can be neglected. In simulations, density bidisperse particles enter the system at a volume feed rate of Q and volume ratio of 1:1. The particle diameter d is uniformly distributed with a variance of $\pm 0.1d$ to reduce crystallization. Particles of 2, 3, and 4 mm diameters are simulated. The flow of mixed particles onto the heap is controlled by a rising gate, which is similar to a letdown tube in industrial systems. The rising gate eliminates bouncing particles caused by free fall of the particles [48], which can influence density segregation dramatically in small systems like this one. The gate, located at $W_F = 0.06$ m, controls the vertical rise velocity $v_r = Q/WT$ of the heap surface. For data analysis, we neglect flow in the feed zone and the area affected by the feed zone which extends to $W_F' \approx 0.15$ m (with small adjustments in different cases), resulting in an effective flowing layer length $L = (W - W_F')/\cos\alpha$. An effective 2D feed

rate can be defined as $q = v_r' L = v_r L \cos\alpha$, where $v_r' = v_r \cos\alpha$ is the rise velocity normal to the free surface. In the moving reference frame of the rising flowing layer, the origin is located on the free surface at W_F'. It is oriented such that x is in the streamwise direction, y is in the thickness direction, and z is normal to the surface of the flowing layer. u, v, and w are the velocities in the x, y, and z directions, respectively.

As in our recent work [39], simulations were performed on an Nvidia GTX 780 graphics card (Graphics Processing Unit) with a parallelized DEM algorithm. Simulations with different feed rates, density ratios, and particle sizes were performed. Details of the kinematics are discussed in §3.

(b) Experiments

To validate the DEM simulations and theoretical predictions, experiments were performed with equal diameters particles with different densities, as indicated in table 1. For each particle type, 100 sample particles were randomly selected and the diameter and the total weight of each was measured. Table 1 lists the average and standard deviation of the diameter and the density calculated by dividing the sum of the volume of each individual particle by the total weight measured for each particle type.

Table 1. Particle properties in experiments.

Material	Color	Diameter (mm)	Density (g/cm^3)
Steel	Dark	2.98 ± 0.04	7.84
Glass	Clear	3.00 ± 0.03	2.58
Ceramic (Zirconium silicate)	White	3.05 ± 0.09	4.17
High density ceramic (Zirconium oxide)	White	3.12 ± 0.10	6.32

The geometry of the experimental system is the same as the simulation geometry ($W = 0.5\,\text{m}$ and $T = 0.016\,\text{m}$). Particle mixtures were held in a hopper and fed into the system by an auger feeder (Acrison, Inc., NJ, USA) at the desired volume feed rate. The rising gate was implemented as a vertical metal bar lifted by a linear actuator (Firgelli Automations Inc., WA, USA) with a control board (Firgelli Technologies Inc, Canada). The experiments were recorded using a high speed camera (Point Grey Research Inc., Canada) with frame rates up to 400 frames/s. Video images were obtained during steady filling of the heap at the downstream end of the flowing layer in contact with the vertical bounding wall and were analyzed to provide concentration profiles of the segregation pattern in the fixed bed and velocity profiles in the flowing layer.

The average image intensity was used to calculate the concentration profile in the streamwise direction for particles in the fixed bed below the flowing layer. The region in figure 2a outlined by the white box was analyzed to characterize the final segregation pattern achieved during steady filling. The boxed image was rotated by the repose angle and sheared into a rectangular domain so that each column of the image has the same streamwise coordinate [48], as shown in figure 2c. The average image intensity at each streamwise location was calculated from the image. Reference image intensities of pure heavy particles and pure light particles were used to calibrate the grey scale.

Particle tracking velocimetry (PTV) was used to determine the velocity profiles in the flowing layer. In this case, the portion of the system to be analyzed extended to the surface of the flow (shifting the box in figure 2a upward so its top edge coincided with the surface of the flowing layer). In close-up images of steady heap flow and with proper lighting conditions, the steel particles can be identified as dark regions with small specular highlights (bright spots) on them, and the ceramic particles can be identified as white or gray spheres. This allows us to apply a MATLAB based PTV code [53] to filter noise and identify the center positions of all the particles (figure 2b). Using a series of images, we computed the velocity of every particle and obtained the streamwise and normal velocity profiles at various locations along the length of the flowing layer
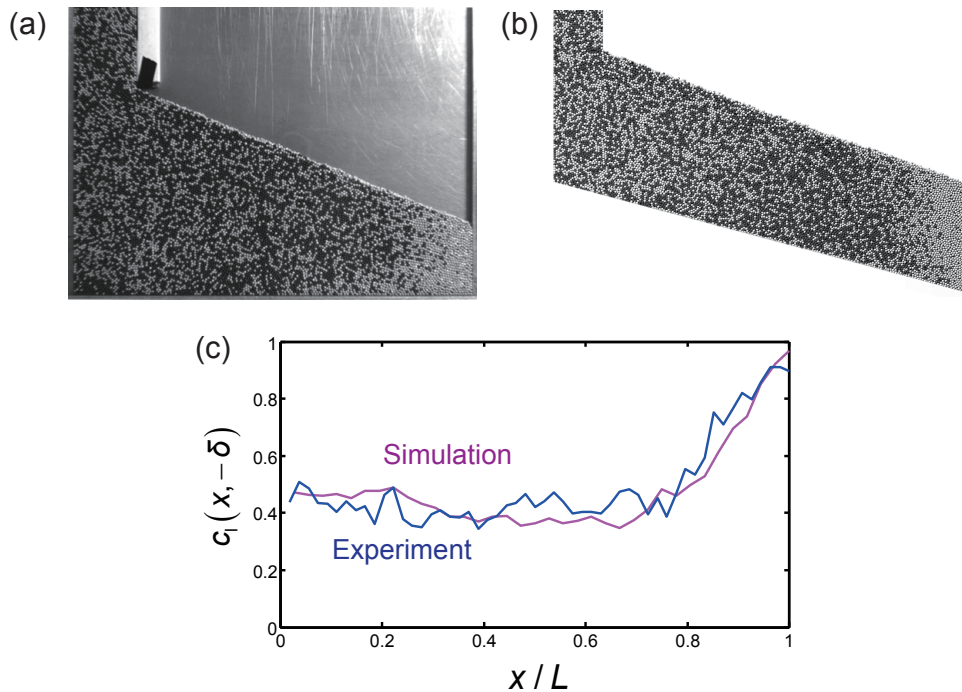
Figure 3. Images comparing segregation in (a) experiment and (b) simulation of lighter ceramic (white) and heavier steel (dark) particles with $q = 0.0032 \, \text{m}^2/\text{s}$. (c) Ceramic particle concentration in the fixed bed beneath the flowing layer.

for steady filling of a steel and ceramic particle mixture. The resulting velocity field was used to validate the simulation results.

(c) Validation of the simulations

Results from a typical DEM simulation and experiment with 3 mm steel and ceramic particles are compared in figure 3. In both cases, the particles are mixed in the inlet region on the left and become more segregated downstream. More ceramic particles flow to the end of the heap forming a region with high ceramic particle concentration. The angle of repose for the simulation ($21.4°$) is also similar to that for the experiment ($22.1°$). A quantitative comparison of light particle concentration (c_l) profiles at the bottom of the flowing layer (deposited on the heap) vs. position (figure 3c) shows good agreement between simulation and experiment, demonstrating that the DEM simulation is able to capture the physics of bidisperse density segregation. Validation of the kinematics of the flow in DEM is described in the next section.

3. Kinematics of density bidisperse flow

(a) Streamwise velocity

The streamwise velocity for the steel and ceramic particle example described in §2c in both simulations and experiments calculated using the volume average binning method [44] is shown in figure 4. Figure 4a shows the free surface streamwise velocity, u_s, along the length
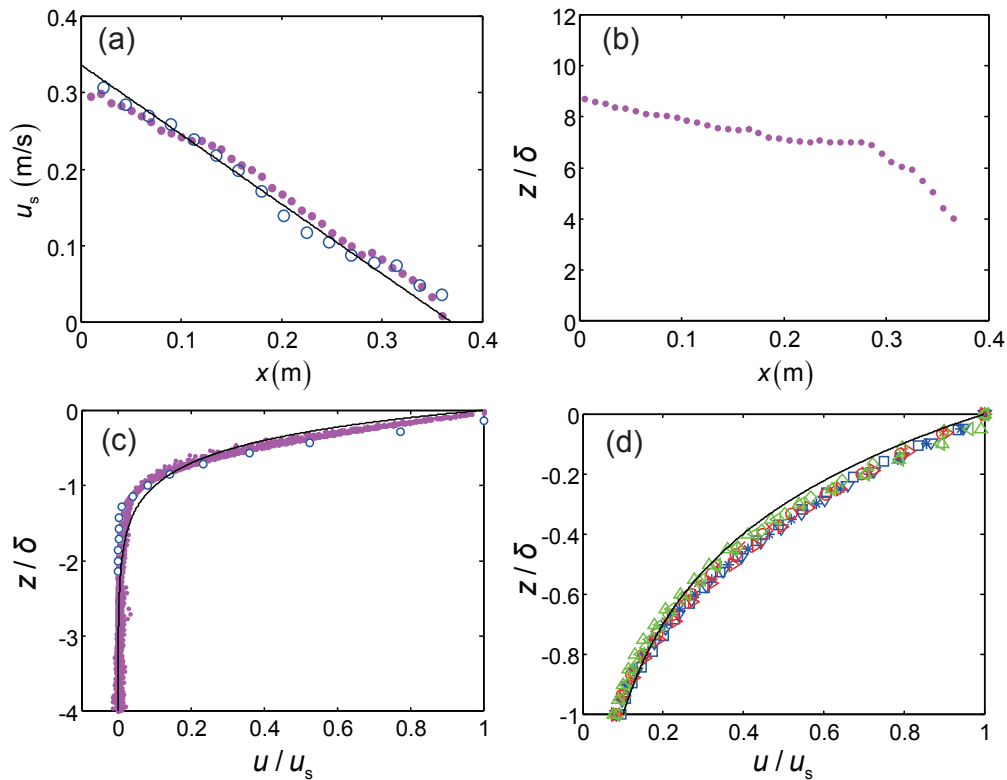
Figure 4. Streamwise velocity profiles in simulation (dots, purple or light gray) and experiment (circles, blue or dark gray), using ceramic and steel particles at feed rate $q = 0.0032\,\mathrm{m^2/s}$. (a) Surface streamwise velocity along streamwise direction. The solid line is $u(x,0) = \frac{kq}{\delta(1-e^{-k})}\left(1 - \frac{x}{L}\right)$. (b) Flowing layer thickness along streamwise direction. (c) Normalized streamwise profile at various positions along the length of the flowing layer. The solid curve is $u/u_s = e^{kz/\delta}$. (d) Streamwise velocity profile at $x/L = 0.5$ for 9 different simulation cases in table 2 collapse on to the solid curve $u/u_s = e^{kz/\delta}$.

of the flowing layer. Results from the experiment and the simulation agree well, exhibiting a nearly linear decrease along the streamwise direction, which is again consistent with a uniform deposition of particles on the heap with an approximately constant flowing layer thickness [44]. Figure 4b shows the flowing layer thickness $\delta(x)$ along the streamwise direction based on the streamwise velocity profile, calculated using the criteria $u(x, -\delta) = 0.1u(x, 0)$ [44]. The flowing layer thickness remains almost constant at 7-8.5 particle diameters for most of the length of the flowing layer, except near the downstream end, again consistent with previous results [44]. For simplicity in the theoretical model, a constant flowing layer depth $\delta = \bar{\delta}$ is assumed, where $\bar{\delta}$ is the average of the flowing layer depth along the entire length of the flowing layer. Based on the local surface velocity and flowing layer depth, the normalized streamwise velocity profiles in the normal direction are plotted in figure 4c for various positions along the length of the flowing layer. The velocity profiles at different streamwise positions in the simulation agree with PTV results and collapse to a single curve, indicating a self-similar exponential velocity profile. The streamwise velocity profiles measured here are consistent with previous results for monodisperse and size bidisperse experiments and simulations [44], so the same exponential expression for the streamwise velocity is used here:
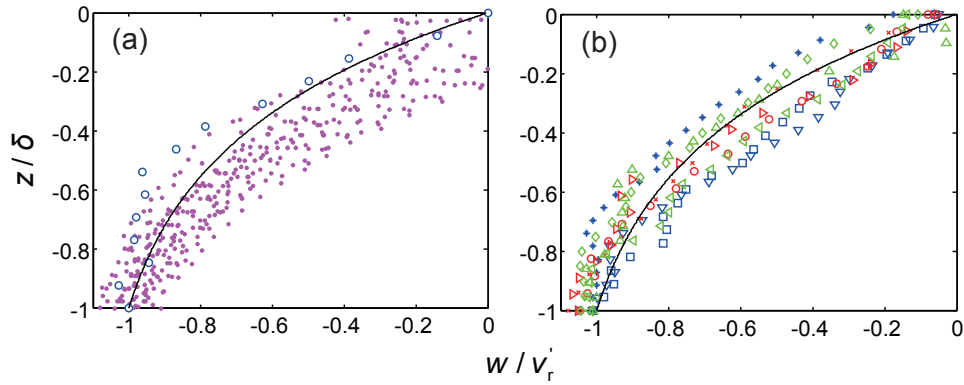
Figure 5. Normal velocity profiles. (a) Normalized normal velocity profiles at various positions along the length of the flowing layer in simulation (dots, purple or light gray), experiment (circles, blue or dark gray), and the predicted normal velocity profile (solid curve) based on the assumption of incompressibility, using ceramic and steel particles at $q = 0.0032\,\mathrm{m}^2/\mathrm{s}$. (b) Normalized streamwise velocity for the nine cases in table 2 at $x/L = 0.5$ collapse onto the predicted velocity profile (solid curve).

Table 2. Nine simulations with different density ratios, feed rates, and particle diameters.

Symbol	R_D	$q\ (\mathrm{m}^2/\mathrm{s})$	$d\ (\mathrm{mm})$
□	1.88	0.0022	3
∗	1.88	0.0041	3
▽	1.88	0.0061	3
×	1.43	0.0022	2
○	1.88	0.0022	2
▷	2.00	0.0022	2
△	1.43	0.0022	4
◇	1.88	0.0022	4
◁	2.00	0.0022	4

$$u(x,z) = \frac{kq}{\delta(1 - e^{-k})} \left(1 - \frac{x}{L}\right) e^{kz/\delta}. \tag{3.1}$$

Equation 3.1 includes a linear decrease in the velocity in the streamwise direction, corresponding to the surface velocity in figure 4a, and an exponential dependence on the normal direction, consistent with the self-similar velocity profiles in figure 4c. Here, k is a scaling constant set to 2.3 [37,44]. To verify the general applicability of equation 3.1, the velocity profiles at $x/L = 0.5$ are plotted in figure 4d for nine simulation cases with different feed rates, density ratios $R_D = \rho_h/\rho_l$, and particle diameters (table 2), along with the exponential fit $u/u_s = e^{kz/\delta}$. The collapse of the data to the exponential fit demonstrates that equation 3.1 describes the self-similar streamwise velocity profiles in the density bidisperse quasi-2D bounded heap flows studied here.

(b) Normal velocity

Using the same method, normal velocity profiles were extracted from the simulations and the experiment. Figure 5a shows a comparison of normal velocities between simulation and experiment for the same case shown in figure 4c. Because normal velocity is typically an order of magnitude smaller than streamwise velocity, the data are more scattered. Yet there is reasonable agreement between the simulation and the experiment. In the coordinate system moving upward with the rise velocity v_r', the normal velocity is zero on the free surface ($z/\delta = 0$) and decreases
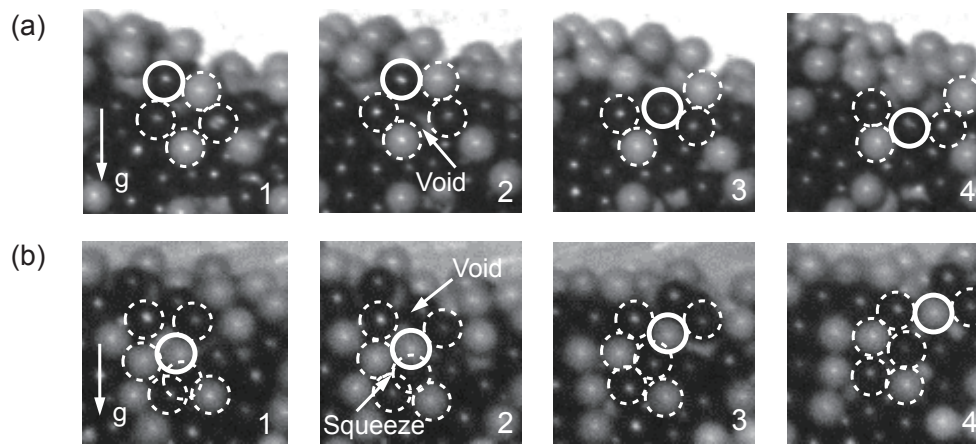
Figure 6. Experimental observation of density segregation of 3 mm particles. (a) A series of images demonstrating a steel particle (solid circle) falling into a void generated by surrounding particles (dashed circles). The time between each image is about 0.015 s. (b) A ceramic particle (solid circle) is squeezed up into a void in the surrounding particles (dashed circles).

to $-v_r'$ at the bottom of the flowing layer ($z/\delta = -1$). Based on equation 3.1 and the continuity equation, the normal velocity is [44]:

$$w(z) = \frac{q}{L(1 - e^{-k})}(e^{kz/\delta} - 1).\qquad(3.2)$$

This equation automatically satisfies the bottom boundary condition $w(-\delta) = -q/L = -v_r \cos\alpha$. To verify this expression, normalized normal velocity profiles at $x/L = 0.5$ for the nine different simulation cases in table 2 are plotted along with $w/v_r' = (e^{kz/\delta} - 1)/(1 - e^{-k})$ in figure 5b. The results from the simulations collapse and are quite similar to the theoretical profile, confirming that equation 3.2 is a reasonable approximation of the normal velocity profiles of density bidisperse flows in quasi-2D bounded heaps.

(c) Segregation velocity

Previous studies of size segregation indicate that kinetic sieving and squeeze expulsion are the dominant segregation mechanisms in gravity driven free surface flows [13,31,32]. Here, analogous phenomena are observed in density bidisperse flows. When voids are generated due to shear, particles with higher density are more likely to fall into voids below them, while particles with lower density are more likely to be squeezed up to voids above them. Two typical examples of these processes from experiment are shown in figure 6. Figure 6a shows a sequence of images in which a steel particle falls into a void generated below it. Figure 6b shows a sequence of images in which a ceramic particle is pushed into a void above it while its original place is taken by a steel particle. An explanation of these phenomena invokes a force imbalance between the gravitational force and contact forces from neighbouring particles, such that a heavier particle on average experiences a net force in the gravitational direction and a lighter particle a net force in the direction opposite gravity. This has been referred to as "buoyancy" in previous studies [20,54].

Though the segregation mechanism at work here results from density differences instead of size differences, the essence of kinetic sieving and squeeze expulsion appears to be similar, and the resulting segregation patterns for density segregation are similar to those for size segregation in quasi-2D bounded heaps [37,39,44,48]. This suggests that the factors that drive density segregation are the same as for size segregation. These factors include the local shear rate,
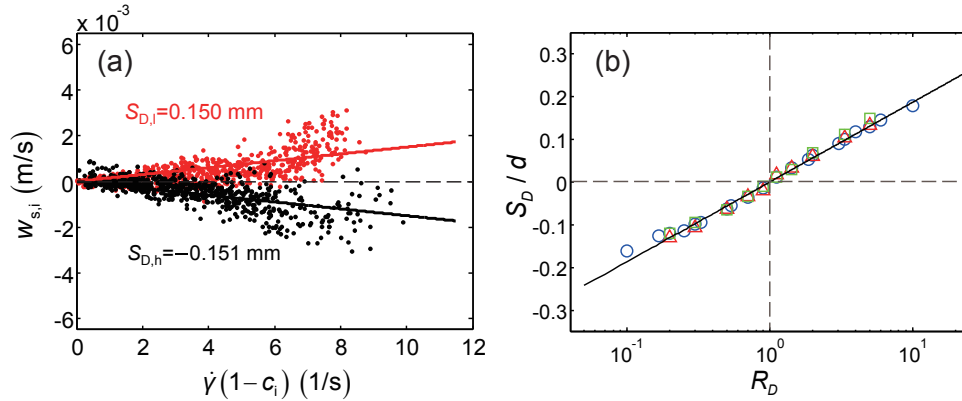
Figure 7. Simulation data for the segregation velocity. (a) Dependence of the segregation velocity on the local shear rate and the local concentration for $R_D = 1.88$, $d = 3\,\mathrm{mm}$ and $q = 0.0032\,\mathrm{m}^2/\mathrm{s}$. Data points and the fitted lines are for light particles (red or light gray) and heavy particles (black). (b) Scaling of density segregation length scale vs. R_D on a semi-log plot for 20 cases of 50:50 mixtures with density ratio R_D ranging from 0.1 to 10, particle diameters of 2 mm (triangles), 3 mm (circles), and 4 mm (squares), and $q = 0.0022\,\mathrm{m}^2/\mathrm{s}$.

$\dot{\gamma} = \partial u / \partial z$, which determines how frequently voids are generated, and the local concentration of the other species, $1 - c_i$, which determines the nature of the contact forces a particle might encounter. To examine the relation between segregation velocity and these factors, the segregation velocity $w_{s,i}$ is plotted as a function of $\dot{\gamma}(1 - c_i)$ for heavy and light particles for an example case in figure 7a. For both light particles and heavy particles, the data suggests an approximately linear relation between $w_{s,i}$ and $\dot{\gamma}(1 - c_i)$, just as for size segregation [37–39]. Consequently, the density segregation velocity can be expressed as:

$$w_{s,i} = S_D \dot{\gamma}(1 - c_i), \tag{3.3}$$

where S_D is the slope of the fitted line for the dependence of $w_{s,i}$ on $\dot{\gamma}(1 - c_i)$, as shown for the example in figure 7a. S_D is analogous to the segregation length in size bidisperse systems [39], and is positive for light particles and negative for heavy particles. For the data in figure 7a, the characteristic length scales for light ($S_{D,l} = 0.150\,\mathrm{mm}$) and heavy ($S_{D,h} = -0.151\,\mathrm{mm}$) particles are nearly identical in magnitude but have opposite signs due to mass conservation [39]. The values for S_D were found for 20 simulation cases using 50:50 mixtures with density ratio R_D ranging from 0.1 to 10 and particle diameters of 2, 3, and 4 mm at $q = 0.0022\,\mathrm{m}^2/\mathrm{s}$. Simulations with different feed rates were also performed, but no significant difference in S_D was found, as expected. As shown in figure 7b, S_D varies with the density ratio R_D and the particle diameter d, in a manner analogous to size segregation [39]. A scaling law for S_D is:

$$\frac{S_D}{d} = C \ln R_D, \tag{3.4}$$

where C is a constant with the value 0.081. 40 data points are shown in figure 7b, since each simulation produces two data points: one for $S_{D,h}$ (corresponding to $R_D > 1$) and one corresponding to $S_{D,l}$ (corresponding to $R_D < 1$). This scaling law differs from the assumed linear dependence of the segregation flux on the density difference $\rho_h - \rho_l$ used in previous studies [20,24].

For DEM simulations with a density ratio $R_D \geq 5$, there is a gradual change in the overall kinematics of the flow in the downstream portion of the heap as R_D increases. At $R_D = 10$ (figure 8), the segregation in the upstream portion of the flow still results from local buoyancy, generating a segregation pattern with strongly segregated regions of light and heavy particles
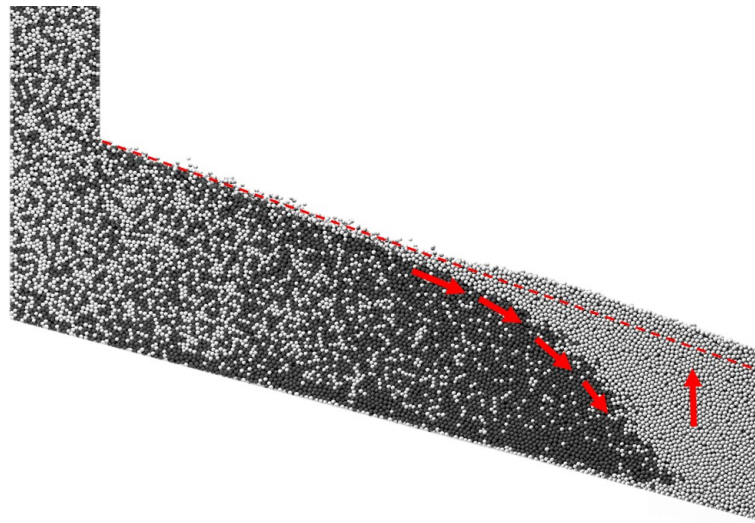
Figure 8. Density segregation at $R_D = 10$, $d = 3\,\mathrm{mm}$, and $q = 0.0040\,\mathrm{m^2/s}$. Heavy particles undercut the light particles toward the end of the heap, pushing light particles upward. The free surface is no longer flat in this case.

having a clear interface in between. However, in the downstream portion a global flow occurs. The resistance of the light particles to the motion of the heavy particles is not significant at this high density ratio, so the heavy particles undercut the light particles toward the end of the heap, pushing the bulk of light particles upward, such that the free surface is no longer flat. Such penetration is analogous to group intruder penetration [55], where the depth of penetration is related to the intruder's speed and density. Since density ratios this large are uncommon in industrial granular flows and this phenomenon introduces more complexity into the kinematics of the flow, we focus on cases with density ratio $R_D \leq 5$ in this study. Note, however, that we are still able to extract local data for density segregation in the flow for $R_D > 5$, thus accounting for these data points in figure 7b.

(d) Diffusion

The diffusion coefficient of the mixture, D, was determined in the normal direction by tracking the non-affine part of particle trajectories using the mean square displacement as a function of time, $\left\langle \Delta Z(\Delta t)^2 \right\rangle$ [37]. The diffusion coefficient was then calculated based on $\left\langle \Delta Z(\Delta t)^2 \right\rangle = 2D\Delta t$ [37, 56]. An example simulation result, shown in figure 9, demonstrates that in density bidisperse flows, the diffusion coefficient is shear rate-dependent, which is consistent with previous studies in dense granular flows [20,56]. In this study, we use the spatial average of the diffusion coefficient over the entire flowing layer domain for the continuum model. We previously showed that for size-disperse granular materials, using the average value of D provides sufficient accuracy to successfully apply the theory, though it is possible to use a locally varying value for D in the theory [37].

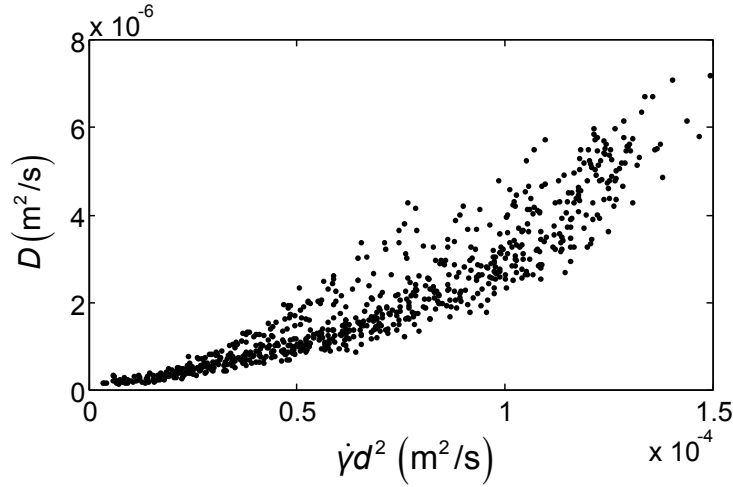## 4. Predictions of the theoretical model

Figure 9. Simulation results for the diffusion coefficient vs. $\dot{\gamma}d^2$ for $R_D = 1.88$, $d = 3\,\mathrm{mm}$, and $q = 0.0032\,\mathrm{m}^2/\mathrm{s}$.

(a) Nondimensionalization and boundary conditions

When applying the transport equation 1.1 to modeling density bidisperse segregation in a quasi-2D bounded heap, it is convenient to nondimensionalize the equation using the nondimensionalized parameters [37,39]

$$\tilde{x} = \frac{x}{L}, \quad \tilde{z} = \frac{z}{\delta}, \quad \tilde{t} = \frac{t}{\delta L/2q}, \quad \tilde{u} = \frac{u}{2q/\delta}, \quad \text{and} \quad \tilde{w} = \frac{w}{2q/L}. \tag{4.1}$$

Substituting the nondimensionalized parameters into equation 1.1 gives the nondimensional transport equation for species i:

$$\frac{\partial c_i}{\partial \tilde{t}} + \tilde{u}\frac{\partial c_i}{\partial \tilde{x}} + \tilde{w}\frac{\partial c_i}{\partial \tilde{z}} \pm \Lambda\frac{\partial}{\partial \tilde{z}}\left[h(\tilde{x}, \tilde{z})c_i(1 - c_i)\right] = \frac{1}{Pe}\frac{\partial^2 c_i}{\partial \tilde{z}^2}. \tag{4.2}$$

In equation 4.2, segregation and diffusion in the streamwise direction x are neglected as assumed previously [20,24,37,38], since these terms are small in comparison with other terms in the equation so long as $\delta/L \ll 1$. The sign of the segregation term is positive for light particles and negative for heavy particles. $h(\tilde{x}, \tilde{z}) = \dot{\gamma}\delta^2/2q$ is the nondimensional shear rate. The Péclet number is $Pe = 2q\delta/DL$, which represents the ratio of a diffusion time scale ($t_d = \delta^2/D$) to an advection time scale ($t_a = L\delta/2q$). The other nondimensional parameter $\Lambda = S_D L/\delta^2$, where $S_D = |S_{D,l}|/2 + |S_{D,h}|/2$, represents the ratio of the advection time scale (t_a) to a segregation time scale ($t_s = \delta^3/2qS_D$). These two nondimensional parameters depend on control parameters (feed rate q and flowing layer length L) and kinematic parameters (flowing layer thickness δ, diffusion coefficient D, and segregation length scale S_D), and they represent the interplay of advection, diffusion, and segregation.

Boundary conditions are also identical to previous studies for size bidisperse flow [37,39]. At the inlet, the particles are well mixed, so $c_l(0, \tilde{z}) = c_h(0, \tilde{z}) = 0.5$. At the top and bottom boundaries of the flowing layer, the segregation flux and diffusion flux are set equal according to the no flux boundary condition suggested by Gray and Chugunov [27], which allows equation 4.2 to be written as

$$\Lambda h(\tilde{x}, \tilde{z})c_i(1 - c_i) = \frac{1}{Pe}\frac{\partial c_i}{\partial \tilde{z}}, \ \tilde{z} = 0, -1. \tag{4.3}$$

The bottom boundary condition ensures that particles leave the flowing layer only due to advection at velocity $w = -v_r\cos\alpha$, and no particles leave the flowing layer at the top surface.
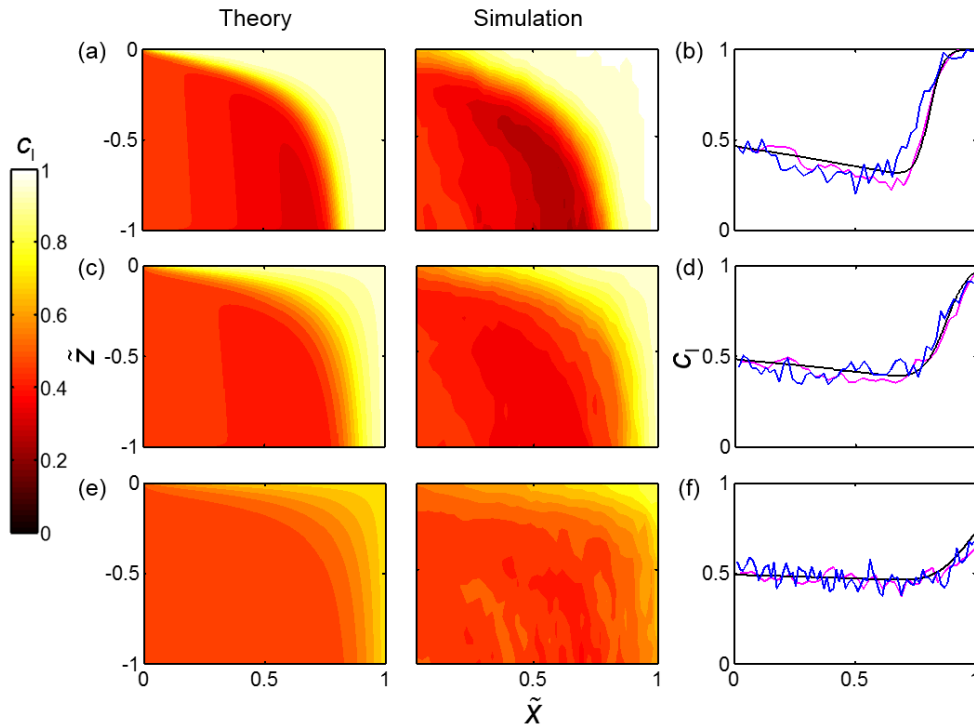
Figure 10. Comparison of theory, simulation, and experiment for density bidisperse segregation with different density ratios. Left and middle columns show concentration contours of light particles in the flowing layer from theory and simulation, respectively. The right column compares theoretical predictions (black), experimental results (blue or dark gray), and simulation results (purple or light gray) at steady state for the concentration profile at the bottom of the flowing layer, which reflects the concentration of the particles deposited on the heap. Top row: glass and steel particles with $R_D = 3.04$, $q = 0.0035\,\mathrm{m^2/s}$, $S_D = 0.29\,\mathrm{mm}$, $D = 2.24\,\mathrm{mm^2 s^{-1}}$, $L = 0.40\,\mathrm{m}$, $\delta = 0.024\,\mathrm{m}$, $Pe = 189$, and $\Lambda = 0.21$. Middle row: ceramic and steel particles with $R_D = 1.88$, $q = 0.0036\,\mathrm{m^2/s}$, $S_D = 0.15\,\mathrm{mm}$, $D = 2.17\,\mathrm{mm^2 s^{-1}}$, $L = 0.40\,\mathrm{m}$, $\delta = 0.023\,\mathrm{m}$, $Pe = 189$, and $\Lambda = 0.12$. Bottom row: high density ceramic and steel particles, with $R_D = 1.24$ and $q = 0.0035\,\mathrm{m^s/s}$, $S_D = 0.05\,\mathrm{mm}$, $D = 2.27\,\mathrm{mm^2 s^{-1}}$, $L = 0.39\,\mathrm{m}$, $\delta = 0.024\,\mathrm{m}$, $Pe = 192$, and $\Lambda = 0.04$.

At the downstream boundary, advection, diffusion, and segregation included in equation 4.2 are in the normal direction. Thus, no boundary condition is needed. With the velocity profiles (equations 3.1, 3.3), equation 4.2 can be solved numerically for steady-state flow using an operator splitting method [37,57,58].

(b) Validation of the theoretical model

To demonstrate that the theoretical model quantitatively predicts bidisperse density segregation in the quasi-2D bounded heap, theoretical, experimental, and simulation results for three example cases with different particle density ratios R_D are shown in figure 10. Each contour subplot (left and center columns) represents the concentration of light particles c_l in the flowing layer extending horizontally from W_F' at $\tilde{x} = 0$ to the end of the flowing layer at $\tilde{x} = 1$ and vertically from the top of the flowing layer at $\tilde{z} = 0$ to the bottom at $\tilde{z} = -1$. Comparing the concentration contours for theory and DEM simulations, it is clear that the theoretical model reproduces the segregation patterns in simulations with good accuracy. In all cases, the particles are well mixed at $\tilde{x} = 0$ and then begin to segregate: heavy particles move toward the bottom of the flowing
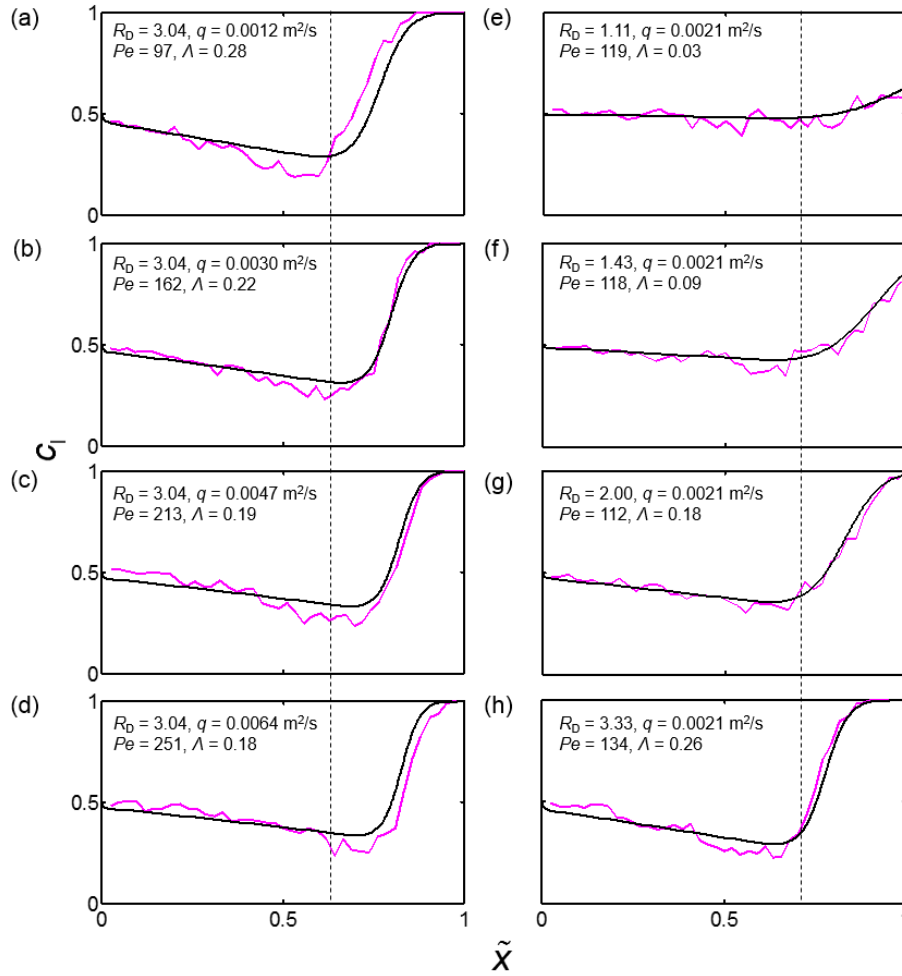
Figure 11. Theoretical predictions (black curves) and simulation results (purple or light gray curves) for the light particle concentration profile at the bottom of the flowing layer, which represent material deposited on the heap. Vertical dashed lines mark the streamwise locations where lowest theoretical concentrations occur in (a) and (e). (a)-(d) Density ratio $R_D = 3.04$ and different feed rates q (labeled on each plot). (e)-(h) $q = 0.0022\,\mathrm{m^2/s}$ and different density ratios R_D (labeled on each plot).

layer to settle out further upstream (smaller $\tilde{x}$), while light particles rise toward the top of the flowing layer and flow further down the heap (larger $\tilde{x}$). The position and shape of the interface between segregated heavy and light particles for the theoretical results agree well with simulation results, indicating that the theoretical model captures the essential physics of density bidisperse segregation. It is also possible to compare the theory and simulation directly with experimental results using the concentration of the light particles, c_l, deposited onto the heap at the bottom of the flowing layer [37], see right column in figure 10. In all three cases, experimental results match the theoretical predictions and simulation results.

The theoretical predictions are determined completely by the two dimensionless parameters Pe and Λ. Pe describes the interplay between advection and diffusion: as Pe becomes larger, advection dominates diffusion, causing the interface between segregated heavy and light particles to become sharper and more easily distinguishable. Λ describes the interplay between segregation and advection. For larger Λ, segregation is stronger so the particles tend to segregate before
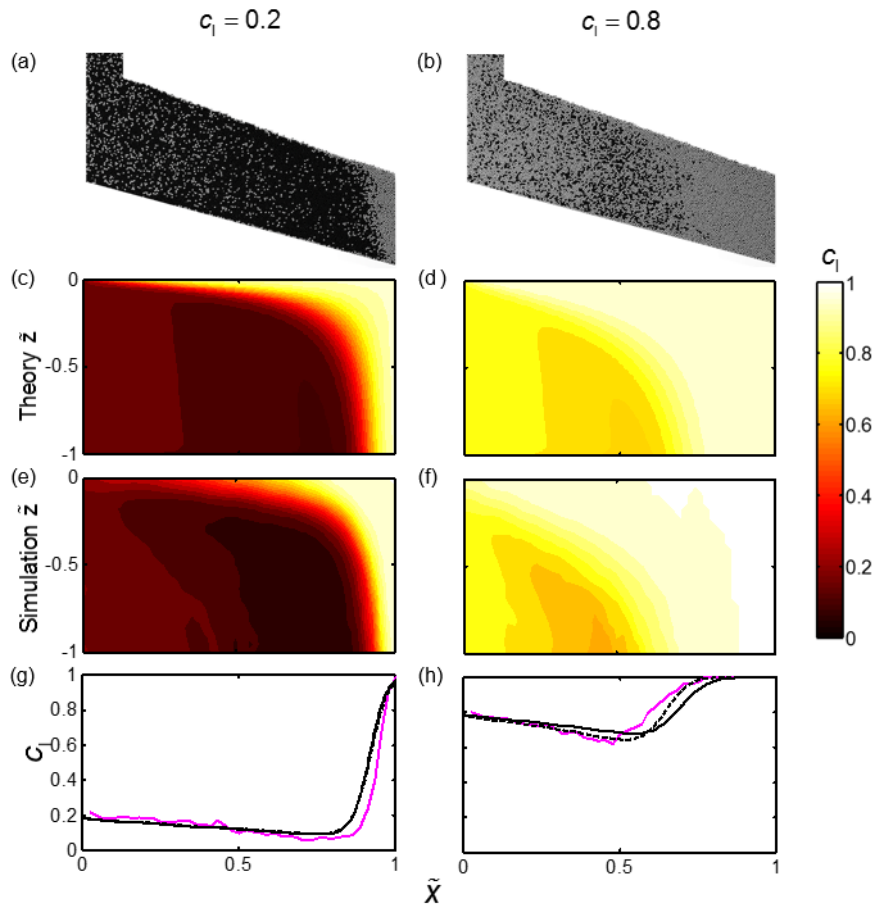
Figure 12. Segregation with different inlet particle concentrations. Left column: inlet light particle concentration $c_l(0, \tilde{z}) = 0.2$, $R_D = 3.04$, $q = 0.0027\,\mathrm{m^2/s}$, $S_D = 0.27\,\mathrm{mm}$, $D = 1.96\,\mathrm{mm^2 s^{-1}}$. $Pe = 146$ and $\Lambda = 0.23$. Right column: inlet light particle concentration $c_l(0, \tilde{z}) = 0.8$, $R_D = 3.04$, $q = 0.0027\,\mathrm{m^2/s}$, $S_D = 0.27\,\mathrm{mm}$, $D = 1.96\,\mathrm{mm^2 s^{-1}}$. $Pe = 143$ and $\Lambda = 0.23$. Row 1: segregation patterns from simulations. Row 2: contours of c_l in the flowing layer from theory. Row 3: contours of c_l in the flowing layer from simulations. Row 4: concentration profiles of light particles at the bottom of the flowing layer from theory (black solid curves for prediction using S_D from equation 3.4, black dashed curves for prediction using S_D measured in each specific simulations) and simulations (pink or light gray curves).

they flow very far down the heap. The influence of these two parameters on segregation has been investigated in detail in the context of size bidisperse systems [37]. Since the form of the theoretical model here is identical to that in previous work for size segregation [37,39] (except that the percolation length scale S is replaced by the density segregation length scale S_D), the discussion is not repeated here.

(c) Predictions of segregation under different physical control parameters

Since Pe and Λ depend on physical control parameters, it is interesting to explore how theoretical predictions of segregation change when the physical control parameters are varied. Among the parameters, density ratio R_D and feed rate q have the greatest influence on the segregation [39]. Figure 11 shows a series of theoretical predictions and simulation results for the concentration

of the light particles at the bottom of the flowing layer (which are deposited on the heap) for different R_D and q. In all cases, D is the average diffusion coefficient based on the simulation for each set of conditions and S_D is from the relation shown in figure 7b. In figures 11a-d, it is clear that increasing q, which results in Pe increasing and Λ decreasing, results in less segregation (the transition from mixed particles to pure light particles occurs further downstream), and a sharper transition between segregated heavy and light particles, which is made more readily apparent in the figures with the aid of a vertical dashed benchmark line. In figures 11e-h, increasing R_D, which results in Λ increasing while Pe varies only a small amount, leads to an obvious increase in segregation, with almost no segregation at $R_D = 1.11$ and strong segregation with $R_D = 3.33$. In all cases, the theoretical predictions match the simulation results well, again demonstrating that the theory is capable of accurately predicting segregation when the physical control parameters are varied.

To further demonstrate the generality of the theory and the form of the segregation velocity, cases with different inlet particle concentrations were simulated and predicted using the theory, as shown in figure 12. In both cases, D is from simulations with $c_l(0, \tilde{z}) = c_h(0, \tilde{z}) = 0.5$ at the same flow rate and the value for S_D is from figure 7b, rather than using these values from the simulations for the $c_l(0, \tilde{z}) = 0.2$ or $c_l(0, \tilde{z}) = 0.8$ cases. The left column shows the case with inlet light particle concentration $c_l(0, \tilde{z}) = 0.2$ and the right column shows the case with $c_l(0, \tilde{z}) = 0.8$. Figures 12a, b show the general segregation patterns in both cases from the DEM simulations. The segregation patterns are consistent with the patterns for 50:50 mixtures shown in figures 3 and 10, in which the heavy particles settle out of the flowing layer in the upstream portion of the heap while the light particles flow further toward the downstream end of the heap. Using the segregation length scale predicted by equation 3.4 ($S_D = 0.27$ mm), the theoretical predictions of the concentration distribution of the light particles in the flowing layer (figures 12c, d) agree reasonably well with the simulation results (figures 12e, f). The comparison of the light particle concentration profiles at the bottom of the flowing layer from simulations and theory (figures 12g, h) demonstrates that the theory is also accurate for particle mixtures with different volume ratios, even when using parameters obtained from a 50:50 mixture.

While examining the effect of different volume ratios on the segregation, we found a difference in the segregation length scale S_D calculated in the simulations with $c_l(0, \tilde{z}) = 0.2$ and $c_l(0, \tilde{z}) = 0.8$ (instead of using equation 3.4). Based on S_D calculated in each simulation, we recalculated Λ (Pe is independent of S_D): $S_D = 0.34$ mm, $\Lambda = 0.28$ for $c_l(0, \tilde{z}) = 0.8$ and $S_D = 0.25$ mm, $\Lambda = 0.21$ for $c_l(0, \tilde{z}) = 0.2$, compared to $S_D = 0.27$ mm, $\Lambda = 0.23$ for $c_l(0, \tilde{z}) = 0.5$. The theoretical predictions using Pe and Λ recalculated in the two cases are also shown in figures 12g, h as dashed curves. For $c_l(0, \tilde{z}) = 0.2$, the new prediction is almost identical to the prediction using S_D from equation 3.4. For $c_l(0, \tilde{z}) = 0.8$, the new prediction shows only a slightly better match to the simulation result. These results indicate that it is reasonable to use equation 3.4 for S_D determined for $c_l(0, \tilde{z}) = 0.5$ even for cases with different inlet concentrations.

The difference in S_D for different inlet concentrations is intriguing, because it indicates that the segregation for a few heavy particles in many light particles is stronger than the segregation for a few light particles in many heavy particles. This is analogous to recent work which shows that small particles segregate faster when surrounded by large particles than vice versa [59,60]. This asymmetry can possibly be explained in terms of the way that a heavy (or small) particle is able to continually push its way downward in the gravitational direction while waiting for a void below it to open when it is surrounded by light (or large) particles. In contrast, a light (or large) particle can only wait for the combination of a void opening above it at the same time as surrounding particles are pushing it upward against gravity when it is surrounded by heavy (or small) particles.

This asymmetry suggests that S_D depends on local particle concentrations. To further explore this, nine simulations with $R_D = 3.04$, and $q = 0.0027 \, \text{m}^2/\text{s}$, and $d = 2$ mm were performed with the inlet light particle concentration varying from 0.1 to 0.9. The segregation velocity shown in figure 13 includes data from all nine simulations. To reduce the noise, we average the data into
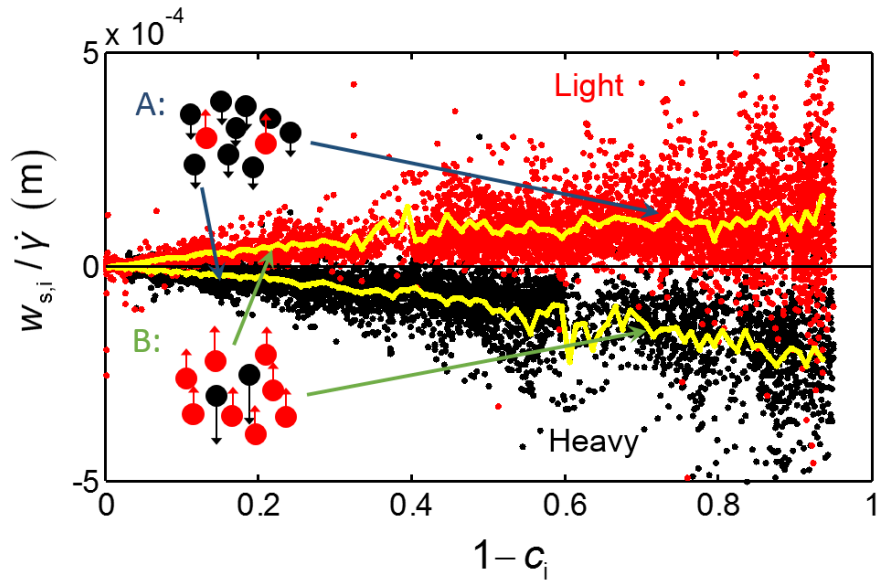
Figure 13. Averaged dependence of segregation velocity on the local shear rate and the local concentration from nine simulations with inlet light particle concentrations ranging from 0.1 to 0.9. In all the cases, $R_D = 3.04$, and $q = 0.0027\,\mathrm{m}^2/\mathrm{s}$, and $d = 2\,\mathrm{mm}$. The data was initially extracted as in figure 7, and then averaged in 100 equal-sized bins along the horizontal axis. The original data extracted from the nine simulation cases (red dots for light and black dots for heavy) and the bin-averaged values for both species (yellow lines) are shown. Data for $c_i \leqslant 0.05$ are neglected because there are too few particles (species i) to get well-averaged data. Case A refers to large $1 - c_i$ in the light particle curve and small $1 - c_i$ in the heavy particle curve. Case B refers to small $1 - c_i$ in the light particle curve and large $1 - c_i$ in the heavy particle curve.

100 equal-sized bins along the horizontal axis, and the averaged results are also shown in figure 13 as two yellow curves. The data for different inlet light particle concentrations are consistent with each other, forming two continuous curves (one for light particles and one for heavy particles). Upon close examination, the curve for the heavy particles, when compared to the curve for light particles, has a slightly smaller slope when $1 - c_i$ is small, corresponding to a high local concentration of heavy particles (case A in the figure), and a slightly larger slope when $1 - c_i$ is large, corresponding to a lower local concentration of heavy particles (case B in the figure). This asymmetry in density segregation reveals the reason for the difference in S_D measured in cases with different inlet light particle concentrations: S_D for $c_l(0, \tilde{z}) = 0.2$ was measured mainly using data from case A, and thus it is smaller than S_D measured for $c_l(0, \tilde{z}) = 0.8$, which mainly used data from case B. Although this asymmetry suggests a slightly non-linear relation between the segregation velocity and the concentration, the theoretical predictions using the linear approximation still show quantitative agreement with simulation results, as figure 12 demonstrates. Clearly, this asymmetry could be taken into account in the theory by using S_D that is a function of c_i, and more work is needed to fully explore this phenomenon.

5. Conclusions

In this study we have demonstrated that our recent continuum model for size bidisperse systems [37–39] accurately predicts granular segregation for density bidisperse systems, specifically for bounded heap flow, though it is likely applicable to other flow geometries and multi- or polydisperse particle distributions, as we have already shown for size segregation [38,40]. Using

experimental techniques and DEM simulations to investigate the kinematics, we developed an approximation for the segregation velocity that depends on local shear rate $\dot{\gamma}$, local concentration of the other species $1 - c_i$, and a dimensional parameter defined as the density segregation length S_D, which depends primarily on the density ratio R_D and, to a lesser extent, on the local particle concentration. The model is based on the transport equation and includes the interplay of advection, diffusion, and segregation. In the model, no arbitrary fitting parameters are needed as the system configurations are determined by two dimensionless parameters $Pe = 2q\delta/DL$ and $\Lambda = S_D L/\delta^2$, which depend only on physical control parameters and kinematic parameters measured from simulations (or experiments, if available). The theoretical predictions quantitatively agree with results from both simulations and experiments under different physical control parameters.

Compared to our model for size segregation [37,39], the primary difference in this study is the segregation length scale in the equation for the segregation velocity, which is related to the density ratio here, as opposed to the size ratio for size segregation. However, apart from this constant, the two models are identical and the resulting segregation patterns for size and density segregation are very similar. This suggests that although the driving force for granular segregation is different in the two cases, the shear-generated segregation mechanism for gravity driven free surface flows is similar. This also suggests that the model has potential to predict combined size and density segregation [24,35]. The asymmetry observed in density segregation for different inlet concentrations indicates that more accurate predictions will require that variations of S_D with concentration be included in the theoretical model. Moreover, the model is not limited to quasi-2D bounded heaps. With proper kinematic information, which is not difficult to acquire, the model should accurately predict density segregation in chutes, tumblers, unbounded heaps, and even 3D geometries.

References

1. Drahun JA, Bridgwater J. 1983 The mechanisms of free surface segregation. *Powder Technol.* **36**, 39-53. (doi:10.1016/0032-5910(83)80007-2)
2. Hill K, Caprihan A, Kakalios J. 1997 Bulk segregation in rotated granular material measured by magnetic resonance imaging. *Phys. Rev. Lett.* **78**, 50. (doi:10.1103/PhysRevLett.78.50)
3. Ottino JM, Khakhar DV. 2000 Mixing and segregation of granular materials. *Annu. Rev. Fluid Mech.* **32**, 55-91. (doi:10.1146/annurev.fluid.32.1.55)
4. Meier SW, Lueptow RM, Ottino JM. 2007 A dynamical systems approach to mixing and segregation of granular materials in tumblers. *Adv. Phys.* **56**, 757-827. (doi:10.1080/00018730701611677)
5. Ahmad K, Smalley IJ. 1973 Observation of particle segregation in vibrated granular systems. *Powder Technol.* **8**, 69-75. (doi:10.1016/0032-5910(73)80064-6)
6. Knight JB, Jaeger HM, Nagel SR. 1993 Vibration-induced size separation in granular media: The convection connection. *Phys. Rev. Lett.* **70**, 3728-3731. (doi:10.1103/PhysRevLett.70.3728)
7. Huerta D, Ruiz-Suárez J. 2004 Vibration-induced granular segregation: a phenomenon driven by three mechanisms. *Phys. Rev. Lett.* **92**, 114301. (doi:10.1103/PhysRevLett.92.114301)
8. Muzzio FJ, Shinbrot T, Glasser BJ. 2002 Powder technology in the pharmaceutical industry: the need to catch up fast. *Powder Technol.* **124**, 1-7. (doi:10.1016/S0032-5910(01)00482-X)
9. Santomaso A, Olivi M, Canu P. 2004 Mechanisms of mixing of granular materials in drum mixers under rolling regime. *Chem. Eng. Sci.* **59**, 3269-3280. (doi:10.1016/j.ces.2004.04.026)
10. Iverson RM. 1997 The physics of debris flows. *Rev. Geophys.* **35**, 245-296. (doi:10.1029/97RG00426)
11. Mitani NK, Matuttis HG, Kadono T. 2004 Density and size segregation in deposits of pyroclastic flow. *Geophys. Res. Lett.* **31**. (doi:10.1029/2004GL020117)

12. Saxton J, Fralick P, Panu U, Wallace K. 2008 Density segregation of minerals during high-velocity transport over a rough bed: implications for the formation of placers. *Econ. Geol.* **103**, 1657-1664. (doi:10.2113/gsecongeo.103.8.1657).

13. Savage S, Lun C. 1988 Particle size segregation in inclined chute flow of dry cohesionless granular solids. *J. Fluid Mech.* **189**, 311-335. (doi:10.1017/S002211208800103X)

14. Khakhar DV, McCarthy JJ, Ottino JM. 1997 Radial segregation of granular mixtures in rotating cylinders. *Phys. Fluids* **9**, 3600-3614. (doi:10.1063/1.869498)

15. Hsiau S-S, Chen W-C. 2002 Density effect of binary mixtures on the segregation process in a vertical shaker. *Adv. Powder Technol.* **13**, 301-315. (doi:10.1163/156855202320252462)

16. Burtally N, King P, Swift MR. 2002 Spontaneous air-driven separation in vertically vibrated fine granular mixtures. *Science* **295**, 1877-1879. (doi:10.1126/science.1066850)

17. Yang SC. 2006 Density effect on mixing and segregation processes in a vibrated binary granular mixture. *Powder Technol.* **164**, 65-74. (doi:10.1016/j.powtec.2006.02.007)

18. Shi Q, Sun G, Hou M, Lu K. 2007 Density-driven segregation in vertically vibrated binary granular mixtures. *Phys. Rev. E* **75**, 061302. (doi:10.1103/PhysRevE.75.061302)

19. Tai CH, Hsiau SS, Kruelle CA. 2010 Density segregation in a vertically vibrated granular bed. *Powder Technol.* **204**, 255-262. (doi:10.1016/j.powtec.2010.08.010)

20. Tripathi A, Khakhar DV. 2013 Density difference-driven segregation in a dense granular flow. *J. Fluid Mech.* **717**, 643-669. (doi:10.1017/jfm.2012.603)

21. Jain N, Ottino JM, Lueptow RM. 2005 Regimes of segregation and mixing in combined size and density granular systems: an experimental study. *Granul. Matter* **7**, 69-81. (doi:10.1007/s10035-005-0198-x)

22. Liao C, Hsiau S, Nien H. 2014 Density-driven spontaneous streak segregation patterns in a thin rotating drum. *Phys. Rev. E* **89**, 062204. (doi:10.1103/PhysRevE.89.062204)

23. Liao C, Hsiau S, Nien H. 2015 Effects of density ratio, rotation speed, and fill level on density-induced granular streak segregation in a rotating drum. *Powder Technol.* **284**, 514-520. (10.1016/j.powtec.2015.07.030)

24. Tunuguntla D, Bokhove O, Thornton A. 2014 A mixture theory for size and density segregation in shallow granular free-surface flows. *J. Fluid Mech.* **749**, 99-112. (doi:10.1017/jfm.2014.223)

25. Fan Y, Hill, K. 2015 Shear-induced segregation of particles by material density. *Phys. Rev. E* **92**, 022211. (doi:10.1103/PhysRevE.92.022211).

26. Gray JMNT, Thornton A. 2005 A theory for particle size segregation in shallow granular free-surface flows. *Proc. R. Soc. A.* **461**, 1447-1473. (doi: 10.1098/rspa.2004.1420)

27. Gray JMNT, Chugunov V. 2006 Particle-size segregation and diffusive remixing in shallow granular avalanches. *J. Fluid Mech.* **569**, 365-398. (doi:10.1017/S0022112006002977)

28. Gray JMNT, Ancey C. 2009 Segregation, recirculation and deposition of coarse particles near two-dimensional avalanche fronts. *J. Fluid Mech.* **629**, 387-423. (doi:10.1017/S0022112009006466)

29. Dolgunin VN, Ukolov AA. 1995 Segregation modeling of particle rapid gravity flow. *Powder Technol.* **83**, 95-103. (doi:10.1016/0032-5910(94)02954-M)

30. Wiederseiner S, Andreini N, Épely-Chauvin G, Moser G, Monnereau M, Gray JMNT, Ancey C. 2011 Experimental investigation into segregating granular flows down chutes. *Phys. Fluids* **23**, 013301. (doi:10.1063/1.3536658)

31. Fan Y, Hill K. 2011 Theory for shear-induced segregation of dense granular mixtures. *New J. Phys.* **13**, 095009. (doi:10.1088/1367-2630/13/9/095009)

32. Thornton A, Weinhart T, Luding S, Bokhove O. 2012 Modeling of particle size segregation: calibration using the discrete particle method. *Int. J. Mod. Phys. C* **23**, 1240014. (doi:10.1142/S0129183112400141)

33. Hajra SK, Shi D, McCarthy JJ. 2012 Granular mixing and segregation in zigzag chute flow. *Phys. Rev. E* **86**, 061318. (doi:PhysRevE.86.061318)

34. Marks B, Rognon P, Einav I. 2012 Grainsize dynamics of polydisperse granular segregation down inclined planes. *J. Fluid Mech.* **690**, 499-511. (doi:10.1017/jfm.2011.454)

35. Gray JMNT, Ancey C. 2015 Particle-size and -density segregation in granular free-surface flows. *J. Fluid Mech.* **779**, 622-668. (doi:10.1017/jfm.2015.438)

36. May LB, Golick LA, Phillips KC, Shearer M, Daniels KE. 2010 Shear-driven size segregation of granular materials: Modeling and experiment. *Phys. Rev. E* **81**, 051301. (doi:10.1103/PhysRevE.81.051301)

37. Fan Y, Schlick CP, Umbanhowar PB, Ottino JM, Lueptow RM. 2014 Modelling size segregation of granular materials: the roles of segregation, advection and diffusion. *J. Fluid Mech.* **741**, 252-279. (doi:10.1017/jfm.2013.680)

38. Schlick CP, Fan Y, Umbanhowar PB, Ottino JM, Lueptow RM. 2015 Granular segregation in circular tumblers: theoretical model and scaling laws. *J. Fluid Mech.* **765**, 632-652. (doi:10.1017/jfm.2015.4)

39. Schlick CP, Fan Y, Isner AB, Umbanhowar PB, Ottino JM, Lueptow RM. 2015 Modeling segregation of bidisperse granular materials using physical control parameters in the quasi-2D bounded heap. *AlChE J.* **61**, 1524-1534. (doi:10.1002/aic.14780)

40. Schlick CP, Isner AB, Freireich BJ, Fan Y, Umbanhowar PB, Ottino JM, Lueptow RM. 2015 A continuum model for segregation of polydisperse granular materials. In revision for *J. Fluid Mech.*

41. Boutreux T, Raphaël E, de Gennes P-G. 1998 Surface flows of granular materials: a modified picture for thick avalanches. *Phys. Rev. E* **58**, 4692. (doi:10.1103/PhysRevE.58.4692)

42. Boutreux T, Makse HA, De Gennes P-G. 1999 Surface flows of granular mixtures. *EPJ B* **9**, 105-115. (doi:10.1007/s100510050746)

43. Khakhar DV, Orpe AV, Andresén P, Ottino JM. 2001 Surface flow of granular materials: model and experiments in heap formation. *J. Fluid Mech.* **441**, 255-264. (doi:10.1017/S0022112001005201)

44. Fan Y, Umbanhowar PB, Ottino JM, Lueptow RM. 2013 Kinematics of monodisperse and bidisperse granular flows in quasi-two-dimensional bounded heaps. *Proc. R. Soc. A* **469**. (doi:10.1098/rspa.2013.0235)

45. Baxter J, Tüzün U, Heyes D, Hayati I, Fredlund P. 1998 Stratification in poured granular heaps. *Nature* **391**, 136-136. (doi:10.1038/34328)

46. Goyal RK, Tomassone MS. 2006 Power-law and exponential segregation in two-dimensional silos of granular mixtures. *Phys. Rev. E* **74**, 051301. (doi:10.1103/PhysRevE.74.051301)

47. Rahman M, Shinohara K, Zhu HP, Yu AB, Zulli P. 2011 Size segregation mechanism of binary particle mixture in forming a conical pile. *Chem. Eng. Sci.* **66**, 6089-6098. (doi:10.1016/j.ces.2011.08.024)

48. Fan Y, Boukerkour Y, Blanc T, Umbanhowar PB, Ottino JM, Lueptow RM. 2012 Stratification, segregation, and mixing of granular materials in quasi-two-dimensional bounded heaps. *Phys. Rev. E* **86**, 051305. (doi:10.1103/PhysRevE.86.051305)

49. Cundall PA, Strack OD. 1979 A discrete numerical model for granular assemblies. *Geotechnique* **29**, 47-65. (doi:10.1680/geot.1979.29.1.47)

50. Shäfer J, Dippel S, Wolf D. 1996 Force schemes in simulations of granular materials. *J. Phys. I* **6**, 5-20. (doi:10.1051/jp1:1996129)

51. Rapaport DC. 2002 Simulational studies of axial granular segregation in a rotating cylinder. *Phys. Rev. E* **65**, 061306. (doi:10.1103/PhysRevE.65.061306)

52. Ristow GH. 2000 *Pattern formation in granular materials*. Berlin, Germany, Springer.

53. Crocker JC, Grier DG. 1996 Methods of digital video microscopy for colloidal studies. *J. Colloid Interface Sci.* **179**, 298-310. (doi:10.1006/jcis.1996.0217).

54. Nichol K, Zanin A, Bastien R, Wandersman E, van Hecke M. 2010 Flow-induced agitations create a granular fluid. *Phys. Rev. Lett.* **104**, 078302. (doi:10.1103/PhysRevLett.104.078302)

55. Pacheco-Vázquez F, Ruiz-Suárez J. 2010 Cooperative dynamics in the penetration of a group of intruders in a granular medium. *Nat. Commun.* **1**, 123. (doi:10.1038/ncomms1123)

56. Utter, B, Behringer, RP. 2004 Self-diffusion in dense granular shear flows. *Phys. Rev. E* **69**, 031308. (doi:10.1103/PhysRevE.69.031308).

57. Christov IC, Ottino JM, Lueptow RM. 2011 From streamline jumping to strange eigenmodes: Bridging the Lagrangian and Eulerian pictures of the kinematics of mixing in granular flows. *Phys. Fluids* **23**, 103302. (doi:10.1063/1.3653280)

58. Schlick CP, Christov IC, Umbanhowar PB, Ottino JM, Lueptow RM. 2013 A mapping method for distributive mixing with diffusion: Interplay between chaos and diffusion in time-periodic sine flow. *Phys. Fluids* **25**, 052102. (doi:10.1063/1.4803897)

59. van der Vaart K, Gajjar P, Epely-Chauvin G, Andreini N, Gray JMNT, Ancey C. 2015 Underlying asymmetry within particle size segregation. *Phys. Rev. Lett.* **114**, 238001. (doi:10.1103/PhysRevLett.114.238001)

60. Golick LA, Daniels KE. 2009 Mixing and segregation rates in sheared granular materials. *Phys. Rev. E* **80**, 042301. (doi:10.1103/PhysRevE.80.042301)